Astrophysics Lab 1:

Measuring the Diameter of Solar System Planets by Interferometry on TELESTO

Joris Josiek

under the supervision of

Prof. Damien Ségransan
Prof. François Bouchy

January 20, 2022

Chapter 1

Introduction

1.1 Context

Interferometry is a commonly used observational technique in astronomy which involves superposing light collected through multiple apertures and making use of its wave-like properties to infer information about angular size of the target source. A typical setup of an interferometer used for professional astronomy can be seen at the Atacama Large Millimeter Array (ALMA) in Chile, which consists of 66 movable telescopes that can be separated by distances of up to 16 km. These large baselines allow us to achieve a much finer resolution compared to just using a single telescope, which constitutes the main advantage of interferometry.

In this project, we will be investigating the possibility of performing interferometry on the Telescope for Science, Teaching and Outreach (TELESTO) installed at the Geneva Observatory in Versoix, Switzerland. TELESTO is a 60 cm Newtonian telescope equipped with a 16 Megapixel CCD image sensor. In order to use the telescope as an interferometer, we will artificially create two apertures by applying a mask to the pupil, effectively reducing the 60 cm aperture to a pair of circles only a few millimeters in diameter.

1.2 Project Overview

As a goal for this project, we will attempt to use interferometry in order to precisely measure the angular diameter of solar system planets. Specifically, the only visible planet with sufficient magnitude given the limited time window of this project was Jupiter. We also have data from observations of Mars taken in 2020, which we will analyze and present in addition to our own observations.

The project is naturally divided into the following three parts.

- <u>Simulations</u>: At this stage, we first run numerical simulations of images produced by observing distant targets through a user-defined interferometric mask. Once we constrain the mask to a more specific shape (double slit experiment), we can analytically compute a

family of functions describing the interference image, whose parameters are related to the physical parameters of the system.

- <u>Observations</u>: This encompasses the practical part of the project of obtaining the desired images using TELESTO. We will describe the workflow of an observation night and also explain the steps needed to preprocess the raw image in order to obtain a final calibrated image which can then be analyzed.

- <u>Data Analysis</u>: In this step, we combine the simulations with the observational data to obtain the parameters of the interference image. In order to fit the analytical functions onto the data, we will use the Metropolis-Hastings algorithm, a type of Markov chain Monte Carlo (MCMC) method, from which we obtain the posterior probability distributions of the parameters involved as well as their correlations.

1.3 Physical Background

The optical setup of this experiment can be described on three planes. A simple interference experiment is exemplified in Figure 1.1. The image plane described by coordinates (u, v) lies on the detector and is where we are measuring the spatial intensity distribution of the incoming light. Note that the instrument focuses the light in such a way that we are actually measuring the angular distribution of intensity so the coordinates u and v have angular (*not* spatial) units.

The mask plane described by coordinates (x, y) is located on top of the telescope. The mask itself can then be considered a transmissivity function m on the (x, y)-plane, where $m = 1$ means full transmission and $m = 0$ means that all light is blocked.

The third plane is the object plane, whose location is so far away from the image plane compared to the mask plane that we can consider it at infinity. This allows us to assume that the incoming light waves are planar, which leads to what is known as *Fraunhofer diffraction*. It yields the following expression for the image field distribution $E(u, v)$ resulting from a plane wave of wavelength λ traveling through a mask $m(x, y)$ at normal incidence.

$$E(u, v) \sim \iint m(x, y)\, e^{-2\pi i (ux + vy)/\lambda}\, \mathrm{d}x\, \mathrm{d}y \tag{1.1}$$

This equation can be derived using geometrical considerations. The aforementioned criteria are met when observing a point source at a perpendicular angle at one specific wavelength. For this reason, the resulting intensity distribution $|E(u, v)|^2$ is known as the Point Spread Function (PSF) of the aperture. The concept of the PSF is fundamental for describing the response of an imaging system and we can use this to build up a theory of imaging a more complex resolved object later.

Finally, we note that the measured field distribution E is essentially a two-dimensional Fourier transform of the mask function m, which is very useful for numerical computations since there exist very efficient algorithms for discrete Fourier transforms, namely the *Fast Fourier Transform* (FFT).
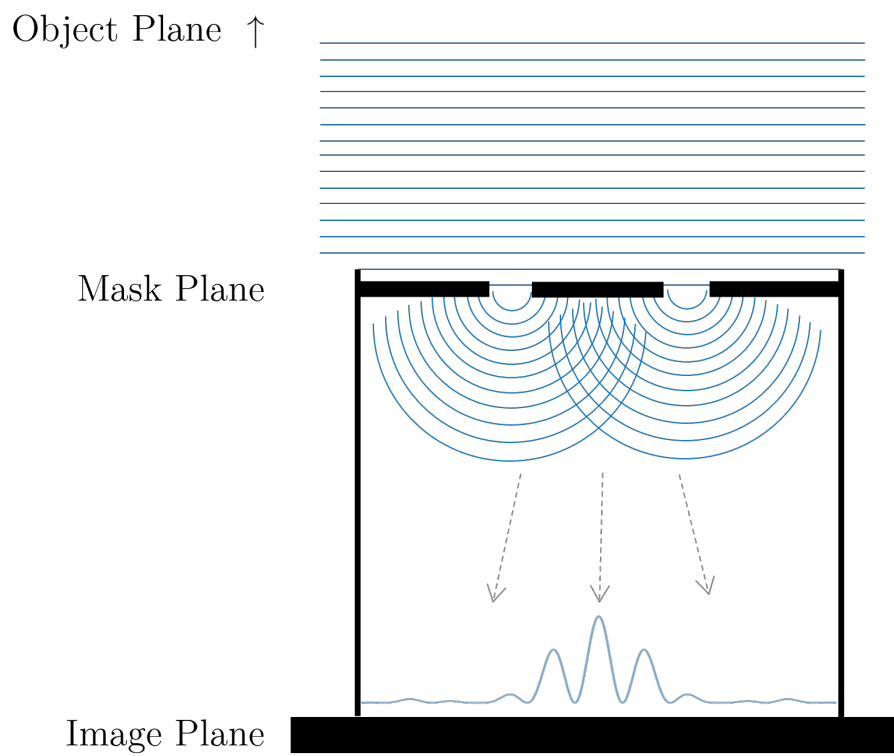
Object Plane ↑

Mask Plane

Image Plane

Figure 1.1: Typical setup of Young's double slit experiment with a one-dimensional mask. Plane electromagnetic waves from infinity hitting the mask plane are diffracted at two different openings, locally creating constructive or destructive interference, finally leading to the depicted interference pattern on the image plane.

Chapter 2

Modeling and Simulations

2.1 Numerical PSF

2.1.1 Units

By Equation 1.1, we can compute the point spread function of any two-dimensional mask numerically with the FFT algorithm, which is included in Python's `numpy` package. However, this package takes discrete axes in units of pixels, so we must carefully consider the physical units of the involved coordinate spaces separately. From the given equation, we see that (u, v) are spatial frequencies of its conjugate space $(x/\lambda, y/\lambda)$. For practical reasons, we would like the image domain to have units of arcseconds. Therefore, we must perform some unit conversion to put the mask space into inverse arcseconds. This is done as follows.

$$x \, [\text{arcsec}^{-1}] \; \widehat{=} \; \frac{x}{\lambda} \times \frac{\pi}{180 \times 3600} \tag{2.1}$$

We can see that the scaling of the axes depends on the wavelength λ. For the simulations, we will use $\lambda = 806 \, \text{nm}$, which corresponds to the center wavelength of the filter we will be using for observations. The conversion for this case is $x \, [\text{arcsec}^{-1}] \approx 6.0151 \times x \, [m]$.

2.1.2 Single Circular Aperture

Consider a telescope with a single circular aperture of diameter D. The single circle mask function is then given by:

$$\text{SC}_D(x, y) := \begin{cases} 1 & \text{for} \quad x^2 + y^2 < \frac{D^2}{4} \\ 0 & \text{else} \end{cases} \tag{2.2}$$

Figure 2.1 shows the PSF of a singular circular aperture for different diameters D. It is apparent that the PSF axes scale inversely to the aperture size. The radius θ of the first local minimum of the PSF, the so called *diffraction limit*, is a fundamental limit on the resolution achievable by the

imaging system and can be approximated by:

$$\theta \approx 1.22 \, \frac{\lambda}{D} \tag{2.3}$$

(a) $D = 3\,\text{mm}$
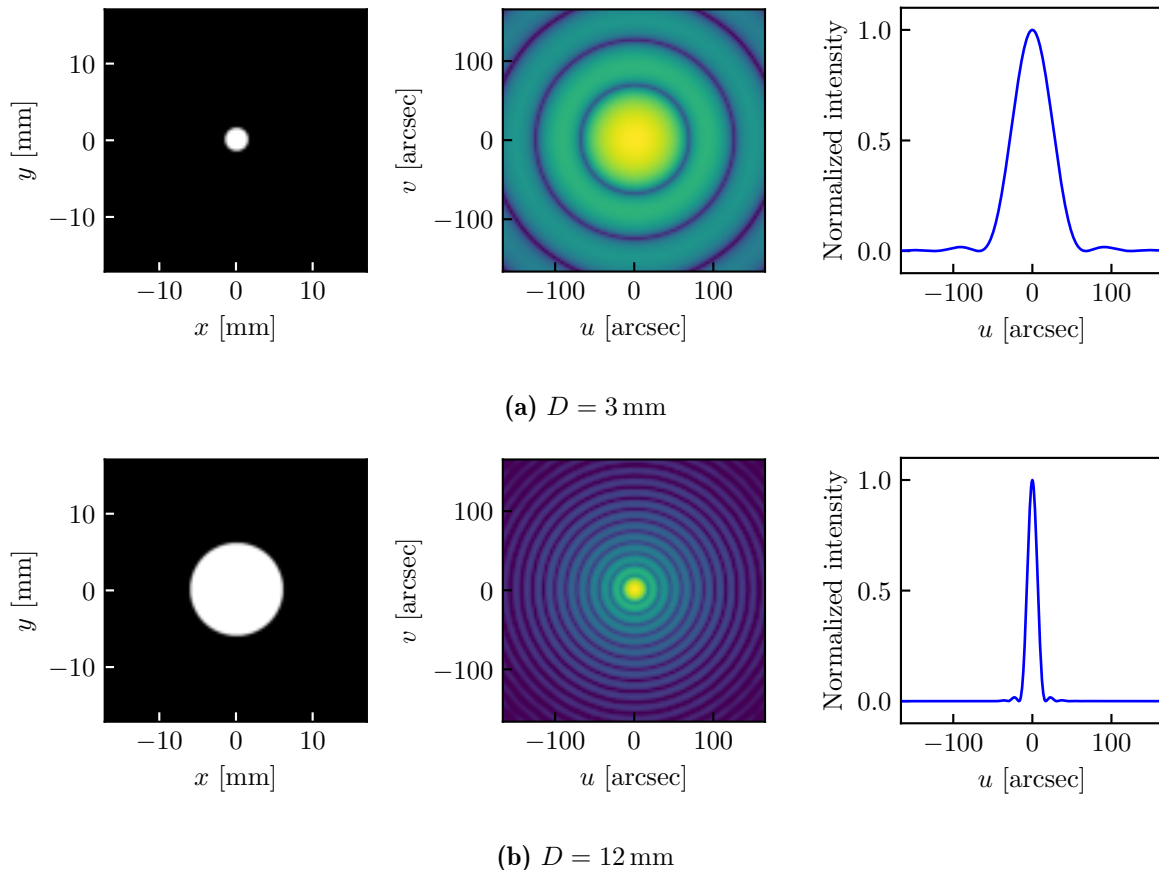

(b) $D = 12\,\text{mm}$

Figure 2.1: Numerically calculated PSF for circular apertures of different diameters. The left images show the aperture shape, the middle images show the PSF with logarithmic color scaling and the right images show a middle cross section thereof with linear scaling.

2.1.3 Double Circular Aperture

Now consider a telescope covered by a mask consisting of two circular apertures of diameter D separated by a distance B (called the *baseline*) along the x-axis (without loss of generality). This setup is described by the following double circle mask function.

$$\text{DC}_{D,B}(x,y) := \begin{cases} 1 & \text{for} \quad (x - \frac{B}{2})^2 + y^2 < \frac{D^2}{4} \text{ or } (x + \frac{B}{2})^2 + y^2 < \frac{D^2}{4} \\ 0 & \text{else} \end{cases} \tag{2.4}$$

Figure 2.2 shows the PSF of a double aperture of diameter $D = 3\,\text{mm}$ at two different baselines. We see that the doubling of the aperture introduces new modulations to the PSF, whose spatial frequency is proportional to the baseline. We will show this more rigorously in the following section where we quantify this PSF analytically.
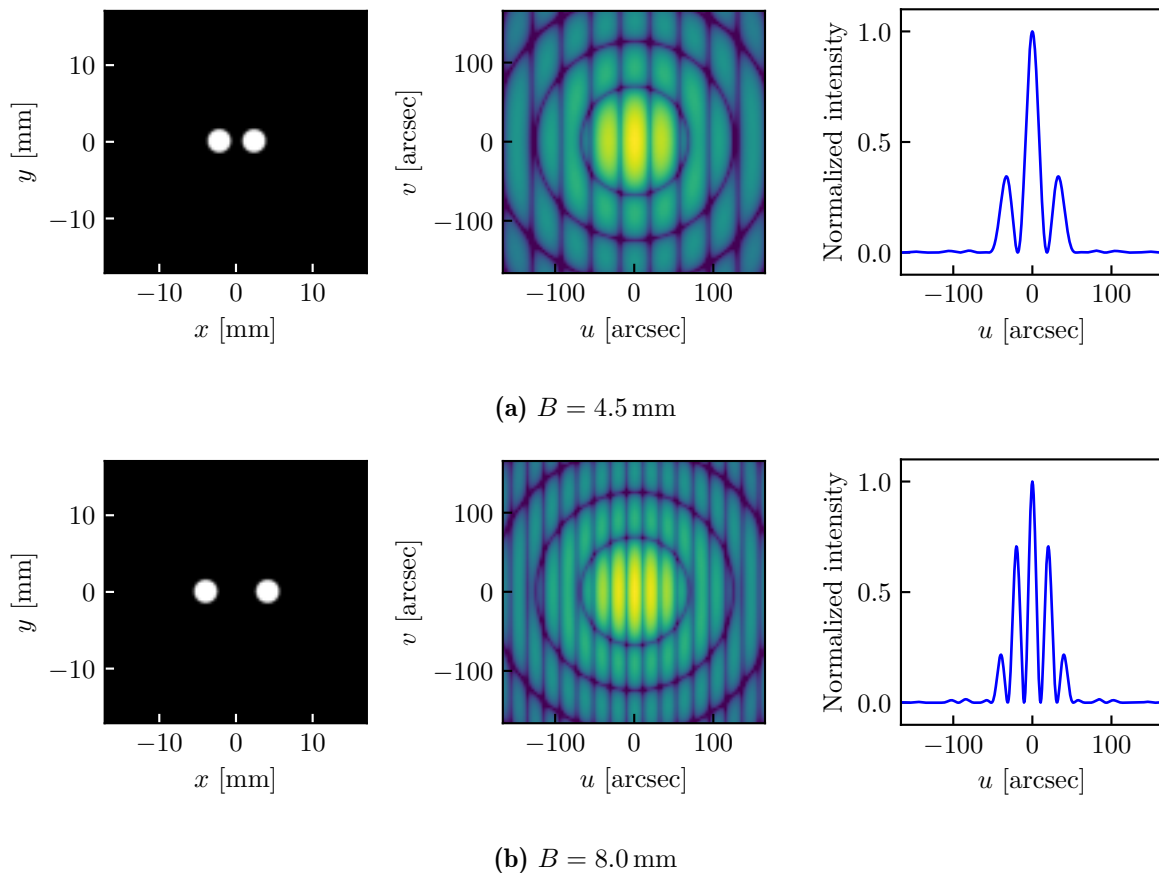
(a) $B = 4.5\,\text{mm}$

(b) $B = 8.0\,\text{mm}$

Figure 2.2: Numerically calculated PSF for double circular apertures of diameter $D = 3\,\text{mm}$ at different baselines. The left images show the aperture shape, the middle images show the PSF with logarithmic color scaling and the right images show a middle horizontal cross section thereof with linear scaling.

2.2 Analytical PSF

For observations, we will use a simple double aperture mask as described in subsection 2.1.3. In order to fit the data, we must model the image as a function of some parameters. Although the numerical method using FFT is theoretically sufficient in order to find parameters of best fit, finding a closed expression greatly increases computing efficiency. In the following section, we will refer to $\vec{x} = (x, y)$ as the coordinate vector in the mask plane and $\vec{u} = (u, v)$ as the coordinate vector in the image plane.

Firstly, that the Fourier transform of the single circle mask SC can be expressed by the order 1 Bessel function of the first kind, denoted by J_1 [1]. Hereby, the circular aperture of unit radius (i.e. diameter $D = 1/2$) has the following Fourier transform.

$$\mathcal{F}[\mathrm{SC}_{1/2}(\vec{x})] = \frac{J_1(2\pi|\vec{u}|)}{|\vec{u}|} \tag{2.5}$$

Thus, the Fourier transform of a circular aperture of any diameter D can be obtained via the Fourier similarity theorem.

$$\mathcal{F}[\mathrm{SC}_D(\vec{x})] = \frac{J_1(\pi D|\vec{u}|)}{|\vec{u}|} \tag{2.6}$$

In order to find the Fourier transform of the double circular aperture, we can make use of the convolution theorem. We note that the double circle mask DC with baseline B and diameter D can be expressed as a convolution of the single circle with two Dirac delta functions.

$$\mathrm{DC}_{D,\vec{B}}(\vec{x}) = \mathrm{SC}_D(\vec{x}) * \left[\delta\left(\vec{x} - \frac{\vec{B}}{2}\right) + \delta\left(\vec{x} + \frac{\vec{B}}{2}\right) \right] \tag{2.7}$$

Here we have generalized the baseline to a two-dimensional vector in order to describe the orientation of the two apertures. This introduces an additional degree of freedom that must be accounted for when fitting the data. We parametrize the baseline vector using polar coordinates, introducing the new parameter ϕ that describes the angle of the line connecting the two openings of the mask with respect to the horizontal.

$$\vec{B} = \begin{pmatrix} B\cos\phi \\ B\sin\phi \end{pmatrix} \tag{2.8}$$

In Fourier space, a convolution becomes a simple multiplication. Therefore, we obtain:

$$
\begin{aligned}
\mathcal{F}[\mathrm{DC}_{D,\vec{B}}(\vec{x})] &= \mathcal{F}[\mathrm{SC}_D(\vec{x})] \times \mathcal{F}\left[\delta\left(\vec{x} - \frac{\vec{B}}{2}\right) + \delta\left(\vec{x} + \frac{\vec{B}}{2}\right) \right] \\
&= \frac{J_1(\pi D|\vec{u}|)}{|\vec{u}|} \times \cos\left(\pi\vec{B}\cdot\vec{u}\right) \\
&= \frac{J_1(\pi D|\vec{u}|)}{|\vec{u}|} \times \cos\left(\pi B(u\cos\phi + v\sin\phi)\right)
\end{aligned}
\tag{2.9}
$$

Introducing a normalization constant N, we now have a closed expression for the PSF of the double circle aperture with diameter D as baseline B oriented at an angle ϕ from the horizontal.

$$\boxed{\mathrm{PSF}_{D,B,\phi,N}[\mathrm{DC}](u,v) = N \times \left(\frac{2J_1(\pi D|\vec{u}|)}{\pi D|\vec{u}|}\right)^2 \times \cos^2\left(\pi B(u\cos\phi + v\sin\phi)\right)} \tag{2.10}$$

This function reproduces the images shown in Figure 2.2. We have added the normalizing coefficient $\frac{2}{\pi D}$ in the Bessel term which makes it tend to 1 in the limit $\vec{u} \to 0$. This is useful

since N then has the intuitive interpretation of being the intensity of the peak maximum. Note that the parameters D and B correspond to lengths in the mask plane but are in units of inverse arcseconds in order to be complementary to the image space (u, v) in arcseconds. The unit transformation must be done as described in subsection 2.1.1 prior to inserting D and B into the equation.

2.3 Resolved Objects

2.3.1 Modeling the Interference Fringes

At this stage, we transition from considering only point sources to computing the interference patterns formed by observing spatially extended objects, as is the ultimate goal of this project. When observing a two dimensional object, each point of that object will individually produce a spatially shifted PSF on the detector. The final image is then the superposition of the PSF of each point normalized by the target's local intensity distribution at that point. Given the (angular) intensity distribution $T(u, v)$ of the target, the final image $I(u, v)$ is then calculated as follows.

$$I(u, v) = \iint \mathrm{PSF}(u - u', v - v')\, T(u', v')\, \mathrm{d}u'\, \mathrm{d}v' = (\mathrm{PSF} * T)(u, v) \qquad (2.11)$$

Practically, this convolution results in the blurring of the interference fringes produced by the double aperture. In order to quantify the fringe contrast, we can introduce a second Bessel function to the PSF in Equation 2.10 so that the cosine is enveloped by a upper *and* lower bound, as shown in Figure 2.3. Let N_1 be the intensity at the center of the image, which is the amplitude of the primary Bessel envelope. Let N_2 be the amplitude of the secondary Bessel envelope. Note that $N_1 > N_2$ if and only if the center is a local maximum.

$$I(u, v) = \left(\frac{2J_1(\pi D|\vec{u}|)}{\pi D|\vec{u}|} \right)^2 \times \left(N_2 + (N_1 - N_2) \cos^2\left(\pi B(u \cos\phi + v \sin\phi) \right) \right) \qquad (2.12)$$

The contrast C is then defined as follows.

$$C := \frac{N_1 - N_2}{N_1 + N_2} \qquad (2.13)$$

Note that in the case $N_1 < N_2$, the contrast is negative by convention. Compare Figure 2.3b and Figure 2.3c to attain a visual intuition for this.

We must now only make one more generalization to the model presented in Equation 2.12 to account for all the degrees of freedom that are not controllable during observation. Namely, we must introduce a possible horizontal translation of the image by a vector $\vec{u}_0 = (u_0, v_0)$, since it will likely not be exactly centered on the detector due to the limited tracking ability of the telescope. The final equation for the image model has the following form.

$$I(u,v) = \left(\frac{2J_1(\pi D|\vec{u} - \vec{u}_0|)}{\pi D|\vec{u} - \vec{u}_0|} \right)^2 \times \left(N_2 + (N_1 - N_2)\cos^2\left(\pi B((u - u_0)\cos\phi + (v - v_0)\sin\phi)\right) \right)$$

(2.14)

There are five parameters $(N_1, N_2, \phi, u_0, v_0)$ which must be determined by a fitting method on the data. The parameters D and B are known constants given by the experimental setup.

2.3.2   Modeling the Visibility Function

Now we must somehow relate the contrast measurement to the diameter of the target. For this, we define the *visibility function* $\mathcal{V}$ of a target as the contrast of the interference fringes as a function of the baseline of the mask. We will make use of the Van Cittert-Zernicke theorem, for which all the conditions are met:

> *"For an incoherent source in quasi-monochromatic conditions, the complex coherence factor* [visibility function] *far from the source is equal to the normalized Fourier transform of its brightness distribution."* [1]

Intuitively, this means that each contrast measurement at one baseline samples the contribution of one spatial frequency in the target's intensity distribution. By measuring the contrast at multiple baselines, we can infer the shape of the target by performing an inverse Fourier transform on the visibility function.

In this project, we will only sample the visibility function at seven different baselines, which means that we will not have sufficient data to reconstruct a detailed image of the observed planets. Therefore, we will make a simplifying assumption that the planets are circular disks of homogeneous brightness. This reduces the multitude of parameters of the object to only one: its diameter d. The Fourier transform of a circular disk with diameter d is already known and the spatial frequencies in Fourier space being the baselines $\vec{B}$, we obtain the model for the visibility function.
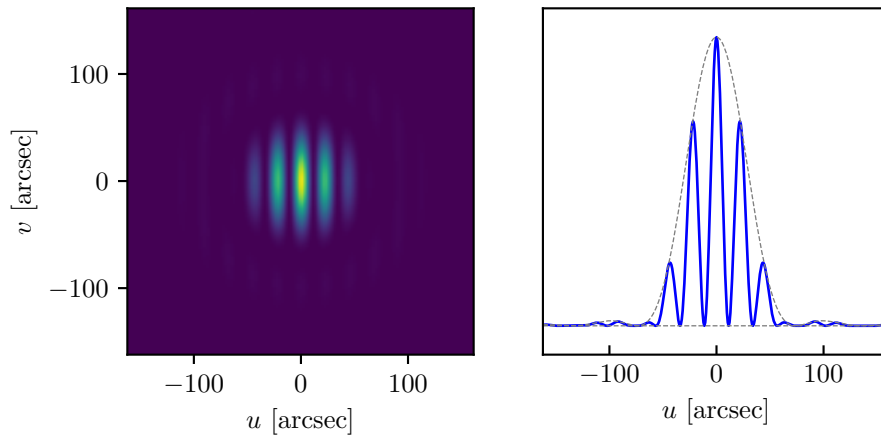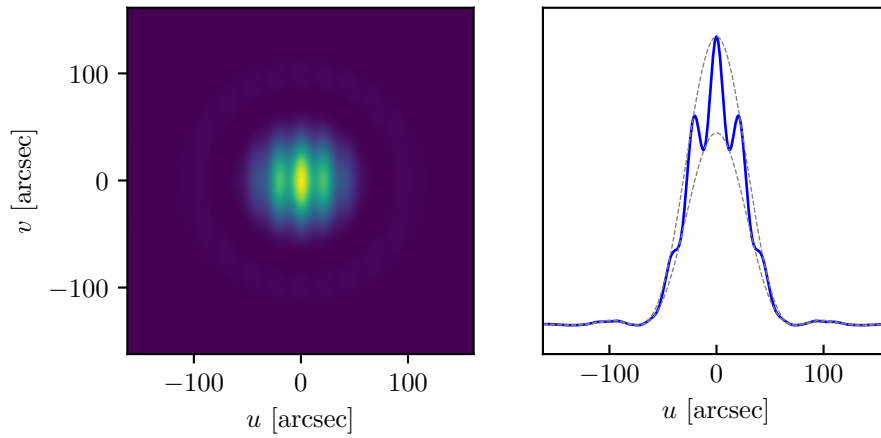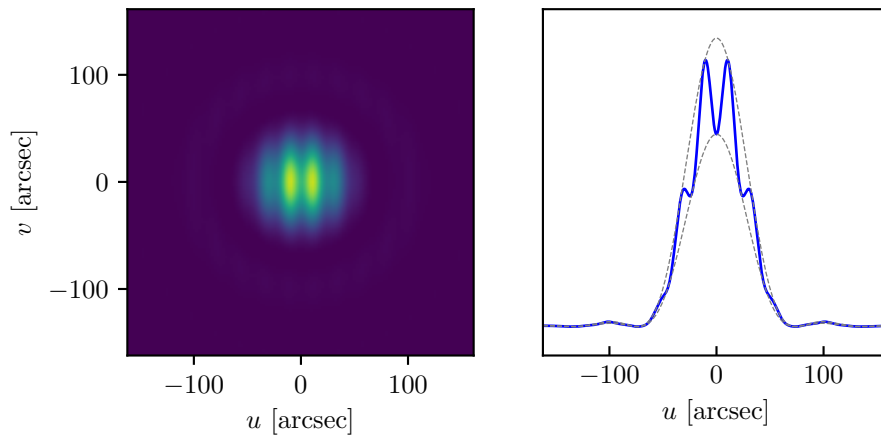
$$\mathcal{V}(B) = \frac{2J_1(\pi dB)}{\pi dB}$$

(2.15)

(a) $C = 100\,\%$ (PSF)

(b) $C = 20\,\%$

(c) $C = -20\,\%$

Figure 2.3: Simulation of fringes with different contrasts though a double circular aperture with $D = 3\,\text{mm}$ and $B = 8\,\text{mm}$. The two-dimensional image with a linear color scale is shown on the left and accompanied by the plot on the right showing the middle horizontal cross section thereof (blue), with the upper and lower Bessel function (gray, dashed).

Chapter 3

Observations

> *Geographical Coordinates of TELESTO:*   *46° 18′ 33.0″* N *6° 08′ 05.8″* E

3.1 Workflow

What follows is a brief description of the steps involved in an observation night, omitting the technical details of operating the telescope. The workspace is shown in Figure 3.1.
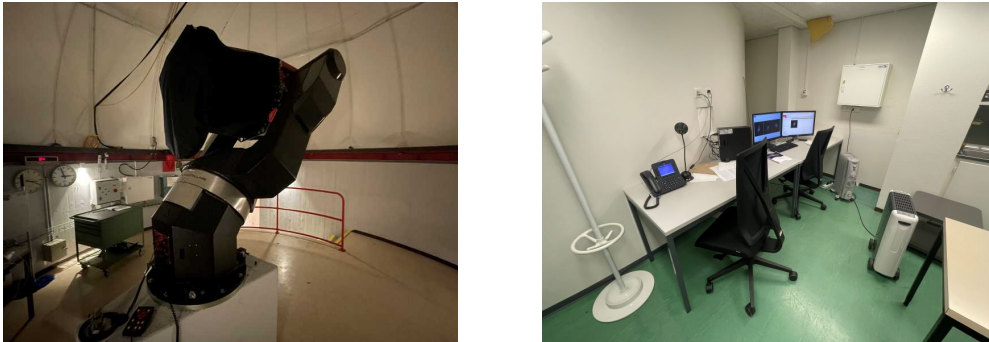

Figure 3.1: Workspace in the TELESTO building. The dome room *(left)* contains the telescope and is accessed in order to open the dome aperture and apply the interferometry mask on the telescope. The camera, filters, shutters and mount rotation of TELESTO are managed via specialized software from the control room *(right)* located below the dome room.

Preparation In advance of a planned observation night, we must verify the observation conditions. There are two aspects to consider. Firstly, we must check the *ephemeris*[1] of the target planet. A good online tool for this is the *Solar System Calculator* created by Don Cross [2]. In order to finish a full run of interferometric observations, we are looking for a time window of about one

---

[1]The *ephemeris* is a table containing information about the apparent trajectory of a celestial object. From this we can extract celestial coordinates at specific observation times.

hour (not including setting up the telescope, starting the software and taking calibration images) where the planet is visible at above 25° elevation. This minimum is due to trees surrounding the TELESTO building.

Secondly, we must check that the weather for the night is optimal. During the wet Geneva winter this is by far the most constraining factor, since the ephemerides of the planets stay relatively unchanged over the course of a few months. A very useful internet site is *meteoblue*, which contains a sub-page that is specialized in weather information for astronomical observations [3]. At an hourly rate for the next three days, it displays the percentage of sky covered by low, mid and high-altitude clouds, as well as two seeing indices quantifying atmospheric turbulence, jet stream speeds, bad layer altitudes and ground temperature.

Aperture Masking   In order to perform interferometric measurements, we must cover the 60 cm pupil of the telescope with a mask. The mask contains two circular openings 5 cm in diameter, one of which we cover completely and in one of which we can insert a small metal disk containing the double circular apertures. There are seven disks we can insert, with baselines ranging between 4.5 mm and 21 mm and an aperture diameter of 3 mm. Figure 3.2 shows this setup.
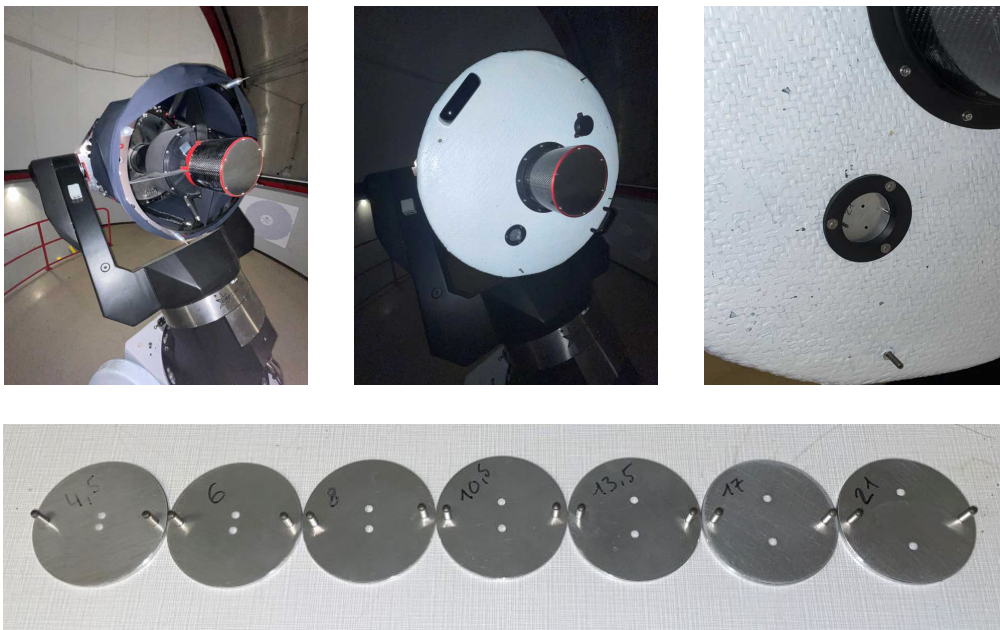

Figure 3.2: Images depicting the basic masking procedure on TELESTO. The opened telescope *(top-left)* is covered with the main mask *(top-center)*, which contains a placeholder for the small metal disk *(top-right)* with the two openings through which the light will ultimately be collected. There are seven disks available covering various baselines *(bottom)*.

Telescope Setup   Using the software installed on the control PC, we can point the telescope at any coordinates and it will automatically track across the sky as the Earth rotates. The software includes a database containing the locations of many celestial objects, including solar system planets, so we practically only need to know the name of the target. We also use the software to

open the shutters on the mirrors and insert a wavelength filter (which we choose from a given palette). Furthermore, the detector in the telescope possesses a thermo-electric cooling system (to reduce thermal noise), whose target temperature we can also adjust in the software. We finally open the dome window after verifying that the dew point is at least a few degrees under the outside air temperature in order to avoid condensation on the mirrors. There are dew point sensors inside the telescope that can be read out from the control PC.

Data Collection   In the software, we can set the exposure parameters and capture either a single image or program an automatic series of images. After exposure, the detector is read out and the collected data is then saved on the computer in the form of a FITS[2] file, which contains the 16-bit brightness value measured at each pixel (known as Analog-to-Digital Units, or ADU) as well as important metadata about the observation including the technical parameters and information about the target. The files can be displayed in open source software such as *SAOImage DS9*. For numerical analysis, the data can be extracted using the `astropy` library in Python.

3.2   Preprocessing

Apart from the main observations of the planetary target, it is also necessary to record some calibration images that will help remove unwanted noise from the main exposures. Cleaning the data is indispensable, especially since the interferometry mask reduces the full aperture area of the telescope by a factor of 20000, forcing us to work with an already low signal-to-noise ratio. There are three types of calibration images to record as part of the preprocessing, which are outlined in the following.

3.2.1   Bias

When the detector is read out after an exposure, the signal produced by photons is offset by intrinsic noise caused by the readout process amplifying the charges deposited on the detector. Each pixel's readout noise fluctuates randomly around some mean value, known as the *bias*. The bias is different from pixel to pixel, which can lead to some systematic error on the overall image. In order to remove this error, one must record a bias image, which is achieved by simply reading out the detector without exposing it first. This is something that can be controlled from within the software. An example bias image is shown in Figure 3.3.

We can further decrease readout noise by decreasing readout speed. The control software lets the user choose a slow readout mode, which operates at 1 million pixels per second. This means that it takes around 16 seconds for one exposure to be recorded.

---

[2]The *Flexible Image Transport System* (FITS) is a digital data storage format that is very commonly used in astronomical imaging.
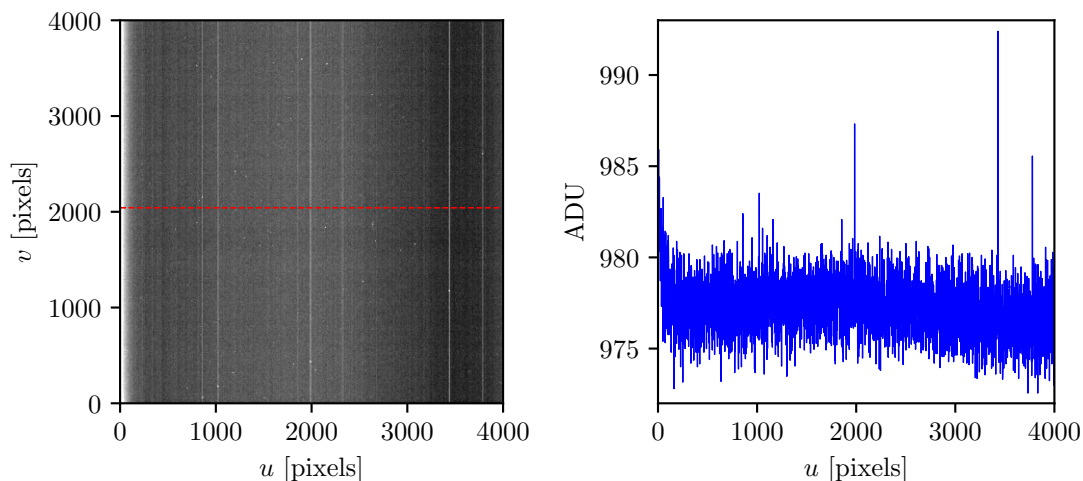
Figure 3.3: Example of a bias image with the brightness profile along a horizontal cut shown by the dashed red line. Although the image consists mainly of white noise, there are patterns such as vertical stripes generated by the detector controller. This is systematic noise that can be removed.

3.2.2 Flat Fielding

The optical configuration of the telescope (including mirrors, focuser and filter) can not distribute light from different angles of incidence homogeneously over the detector. This is in part due to the geometry of the telescope and in part due to dust and deterioration on the optical components affecting the light path. To account for this, we record a *flat frame*, which is an image taken of an evenly lit area that covers the telescope's field of view. Usually, this can be done either on the flat sky just after sunset or on an artificially lit path of the dome's interior. The observational data can be normalized with the flat frame, which equalizes the image by removing the instrumentation effect on the recorded brightness profile. An example flat frame is shown in Figure 3.4.

Note that the flat frame is characteristic of the exact optical setup between the sky and the detector and is therefore filter-dependent. A new flat frame must be recorded for each filter used.

3.2.3 Dark Current

During exposure, charges will be deposited on the detector because of thermal motion within the material. This has nothing to do with photons striking the detector and is therefore known as *dark current*. Even though there is a random component to this, some pixels are more sensitive to thermal noise than others, resulting in a systematic pattern on the image. The dark current can be recorded by exposing an image without opening the shutters on the detector. Since the signal produced by thermal noise is time and temperature dependent, the exposure time and detector temperature of the dark current image must match those of the observation.

The detector temperature can be controlled with a thermo-electric cooling element, capable of maintaining a temperature as low as $-30°$C (even lower if the night is cold enough). Even though
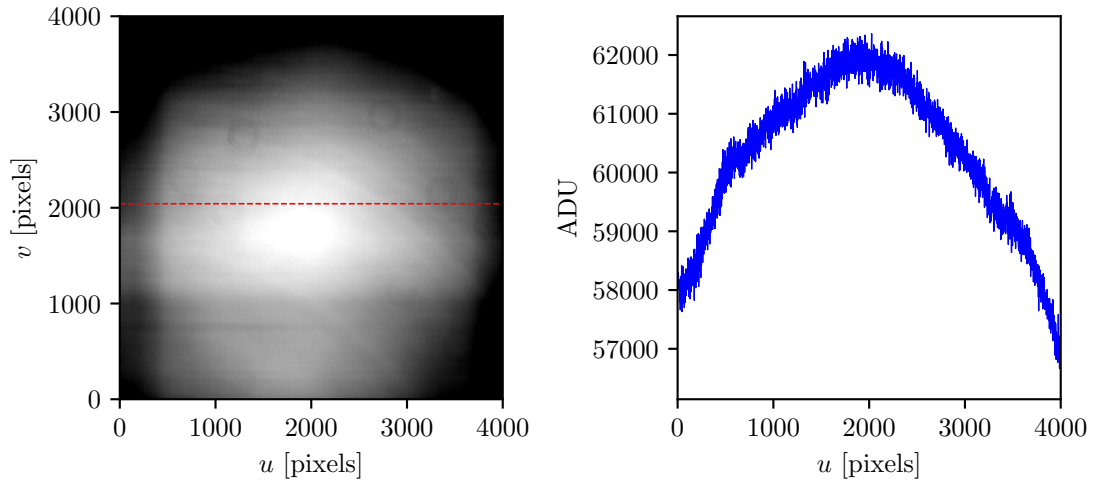
Figure 3.4: Example of a flat frame with the brightness profile along a horizontal cut shown by the dashed red line. The dominant feature is vignetting, which refers to the darkening on the edges of the image.
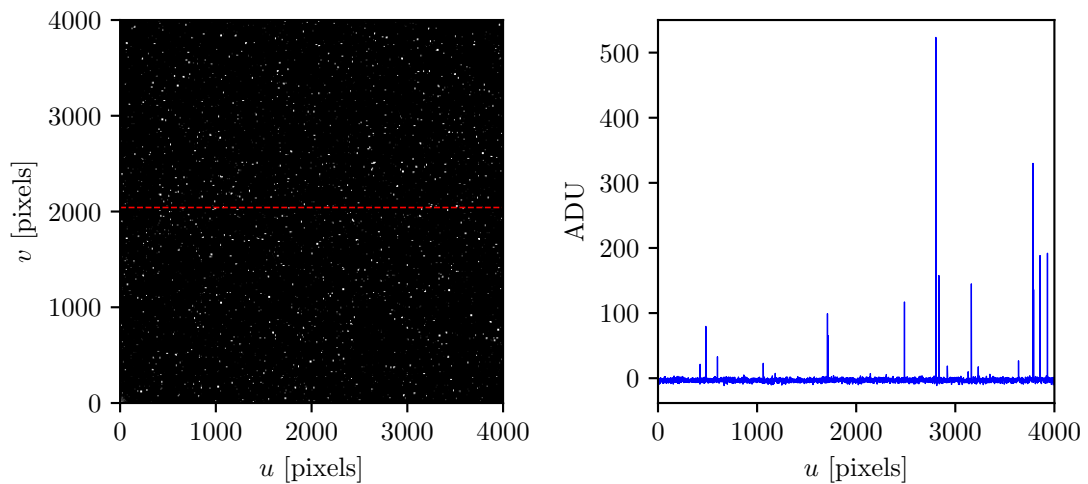

Figure 3.5: Example of a dark current image (bias removed) with the brightness profile along a horizontal cut shown by the dashed red line. The thermal effects manifest themselves as singular bright pixels that can easily be mistaken for stars.

detector cooling helps minimize thermal noise, the long exposure times made necessary by the small aperture make the dark current non-negligible in this experiment.

An example dark current image is shown in Figure 3.5.

3.2.4 Summary of Prepocessing

In reality, we will record about 10 of each type of calibration image to be averaged out into a *master bias*, *master flat* and *master dark*. This is to remove the statistical noise component, which avoids introducing more noise when calibrating the observational images. Note that the flat frames and dark current images themselves must have their bias removed before constructing the master frames. Finally, the observational data is preprocessed according to the following equation.

$$\text{Calibrated Image} = \frac{\text{Raw Image} - \text{Master Bias} - \text{Master Dark}}{\text{Master Flat}} \tag{3.1}$$

3.3 Technical Data

Table 3.1 shows a summary of metadata about the observation.

Aperture diameter:	3 mm
Aperture baselines:	4.5 mm, 6.0 mm, 8.0 mm, 10.5 mm, 13.5 mm, 17.0 mm, 21.0 mm
Detector resolution:	4096×4096
Angular scale:	1 pixel $\widehat{=}$ 0.8 arcsec
Detector temperature:	$-30°$C
Wavelength filter:	I Band [806 nm $\pm$ 149 nm]
Readout speed:	1 MHz
Exposure time:	300 s
Observation date:	12 December 2021, 6–7 pm (Jupiter)
additional data from	18 November 2020, 6–8 pm (Mars)

**Table 3.1:** Technical details of the observations.

3.4   Tracking Stability

The instrumentation problem that is without doubt the main source of error for this project is the tracking issue experienced by the telescope. TELESTO is positioned on top of an equatorial mount, meaning that its primary axis is parallel to the earth's rotational axis. Under functional conditions, the telescope's motorized mount can track a given target across the sky by matching the Earth's angular velocity with its primary axis (which controls the right ascension coordinate). If the positioning of this axis is slightly off, one can calibrate the software to use the secondary axis (declination) to correct for this.

During some preliminary observations, we noticed that the telescope was not able to stay on target for long exposures. To quantify this problem, a series of short exposures of a bright target was recorded and the center location of the target on the image was tracked over time. This produced the data shown in Figure 3.6a. We immediately notice an obvious oscillation in the apparent right ascension of the target with an amplitude of 4 arcsec and period of 5 minutes. Additionally, both coordinates experience a gradual drift over the course of the sequence. The oscillation issue points to mechanical fault in the telescope's motorized rotation, while the drift can probably be attributed to incorrect calibration of the tracking model accounting for an off-parallel positioning of the primary axis.

We repeated the tracking sequence in different directions, one more of which is shown in Figure 3.6b, and obtained more or less similar results, all of which had in common the slight approximately linear drift. However, the amplitude of the oscillation differed significantly on different targets, from being practically zero up to more than 10 arcsec. Furthermore, the amplitude of the oscillation could change *on the same target* when repositioning the telescope from a different direction.

Since the calibration of the telescope's mount requires technical expertise, and the oscillation issue seems to occur unpredictably, we can only try to minimize the effect this has on the interference fringes by placing the mask so that the baseline is perpendicular to the right ascension axis. This way, the fringes will appear parallel to the oscillation, minimizing the effect this has on their contrast. Nevertheless, the tracking stability is not a negligible influence on the results and must be taken into consideration in the discussion.
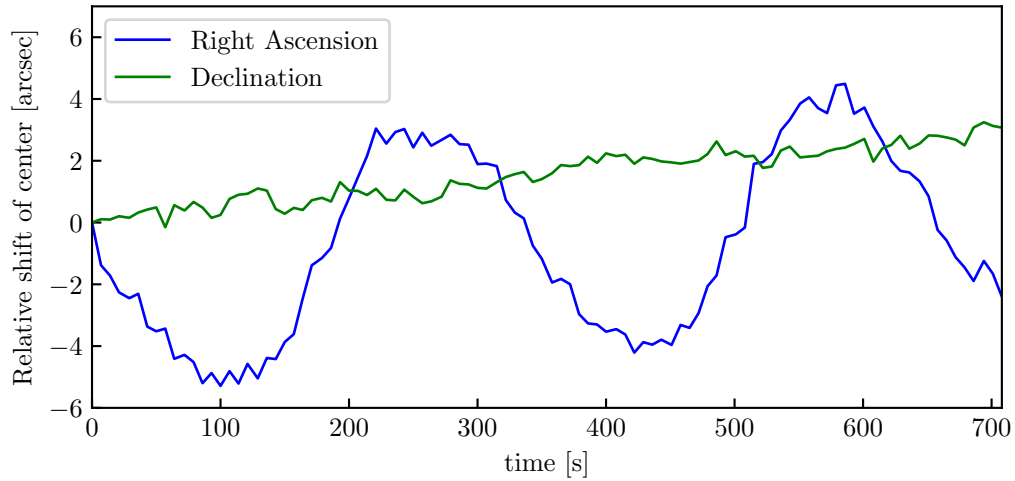
(a) Zenith
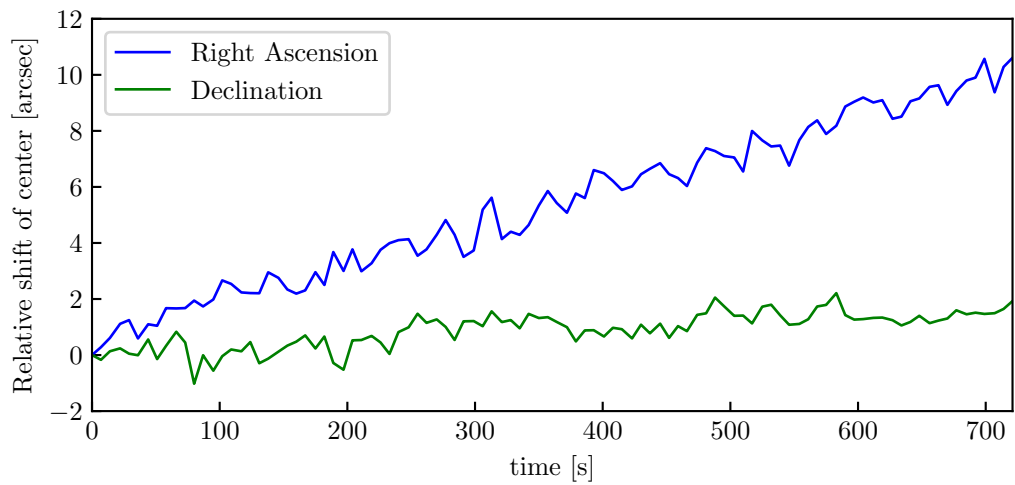
(b) South

Figure 3.6: Apparent equatorial coordinates of the center of a target over time, relative to its position at the beginning of the sequence.

Chapter 4

Data Analysis

Figure 4.1 shows images captured on Jupiter for the seven aperture masks. The data has been preprocessed with the appropriate calibration images and cropped to the relevant area. In addition, we show images captured on Mars previously in Figure 4.2.
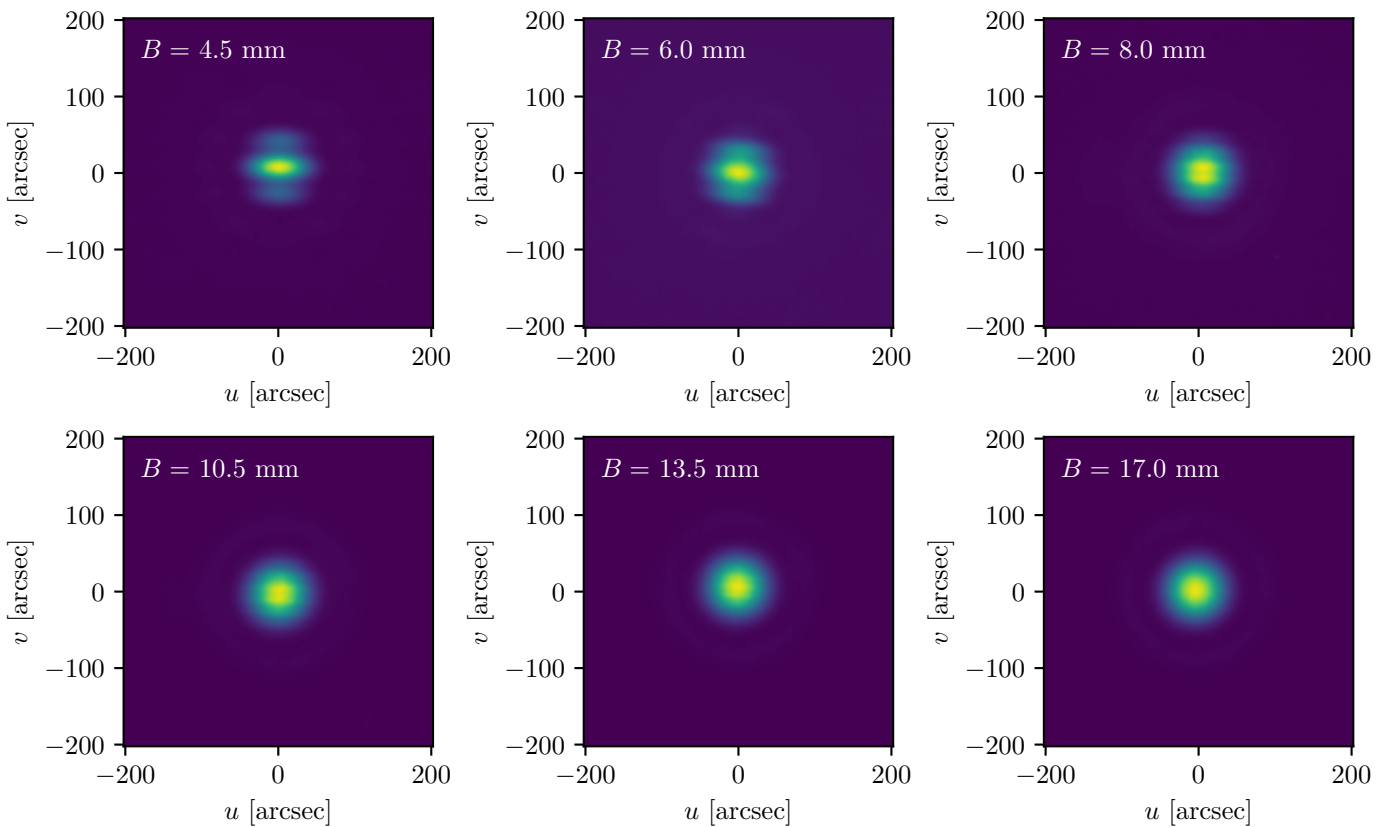

Figure 4.1: Data captured targeting Jupiter with masks at different baselines.
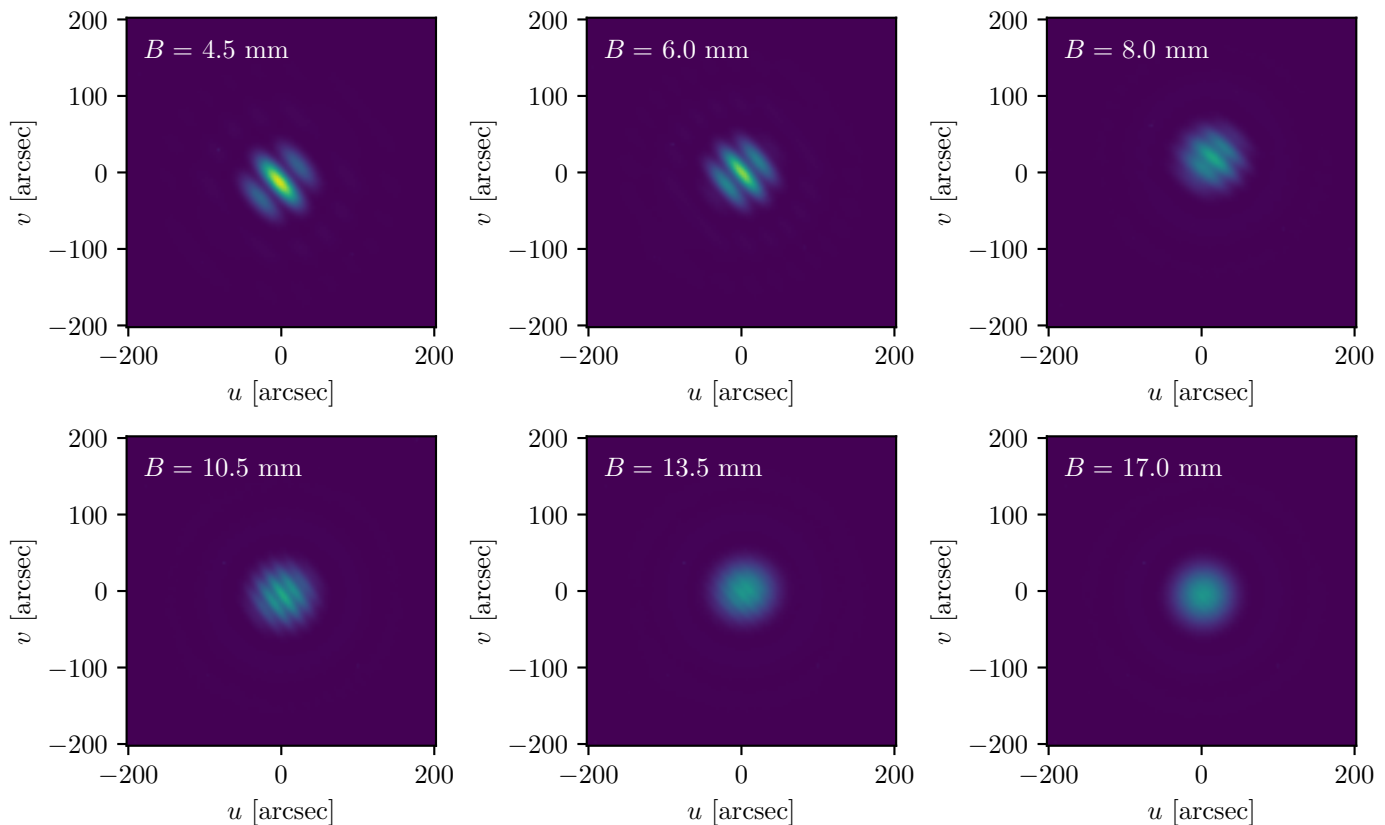
Figure 4.2: Data captured targeting Mars with masks at different baselines. (2020)

4.1 Data Fitting by MCMC

In the following step, we will determine the parameters of the data according to Equation 2.14. To do this, we will use the Scaled Adaptive Metropolis sampling algorithm (`samsam`) [4], a type of Markov chain Monte Carlo (MCMC) method. In summary, this kind of algorithm stochastically samples the desired parameters from their posterior probability distribution based on the likelihood of the given data. With a sufficiently large sample size, the MCMC algorithm yields an approximation of said probability distribution from which we can extract the mean and standard deviation of each parameter. Furthermore, since the algorithm produces the probability distribution on the entire multi-dimensional parameter space (rather than each individual one-dimensional parameter), we can also extract the pairwise correlations between the parameters.

Using an MCMC algorithm requires the definition of a likelihood function, which describes the total probability of obtaining the data given a certain set of parameters $\theta := (N_1, N_2, \phi, u_0, v_0)$. For this, we assume that the brightness measurement is independent from pixel to pixel. Let F_{ij} be the brightness measured at pixel (i, j). The likelihood L is simply the product of the probability of measuring each pixel given the parameters.

$$L(\theta) = \prod_{ij} P(F_{ij}|\theta) \tag{4.1}$$

We assume that P is distributed by a Gaussian centered on the model given by the function F_θ.

$$P(F_{ij}|\theta) = \frac{1}{\sqrt{2\pi\sigma_{ij}^2}} \exp\left(-\frac{(F_{ij} - F_\theta(u_i, v_j))^2}{2\sigma_{ij}^2}\right) \tag{4.2}$$

The error σ_{ij} consists of the readout noise of about $10\,\mathrm{ADU}$ and the Poisson-distributed photon noise whose error is the square root of the measured brightness.

$$\sigma_{ij}^2 = \sigma_{\mathrm{readout}}^2 + \sigma_{\mathrm{photon},ij}^2 = 100 + F_{ij} \tag{4.3}$$

For practical reasons, the algorithm works with the logarithm of the likelihood function to ease numerical computations. The loglikelihood function is then as follows.

$$\log L(\theta) = -\frac{1}{2}\sum_{ij}\log(2\pi(100 + F_{ij})^2) - \sum_{ij}\frac{(F_{ij} - F_\theta(u_i, v_j))^2}{2(100 + F_{ij})} \tag{4.4}$$

4.2 Extracting the Contrast

For the sake of brevity, we will show the method for obtaining a contrast measurement only for baseline $B = 8\,\mathrm{mm}$ on Jupiter. The procedure is analogous for all seven exposures shown in Figure 4.1.

Given the data, the parameter-dependent model function and the resulting likelihood function, the MCMC algorithm proceeds to sample randomly from the posterior probability distribution of the parameters. The histograms as well as correlation plots resulting from this can be plotted with the `corner` package in Python [5], an example of which we have shown in Figure 4.3 for the 8.0 mm baseline. The results show almost no pairwise correlations between the parameters.

The best fit model is given by the mean of each parameter. Figure 4.4 shows the captured data along with the best fit and the residuals ($=$ data $-$ fit). The interference fringes are still visible in the residuals in part because high flux areas are more noisy due to Poisson-distributed photon noise. Additionally, the color scale in the residuals plot is exaggerated in order to highlight the visible patterns.
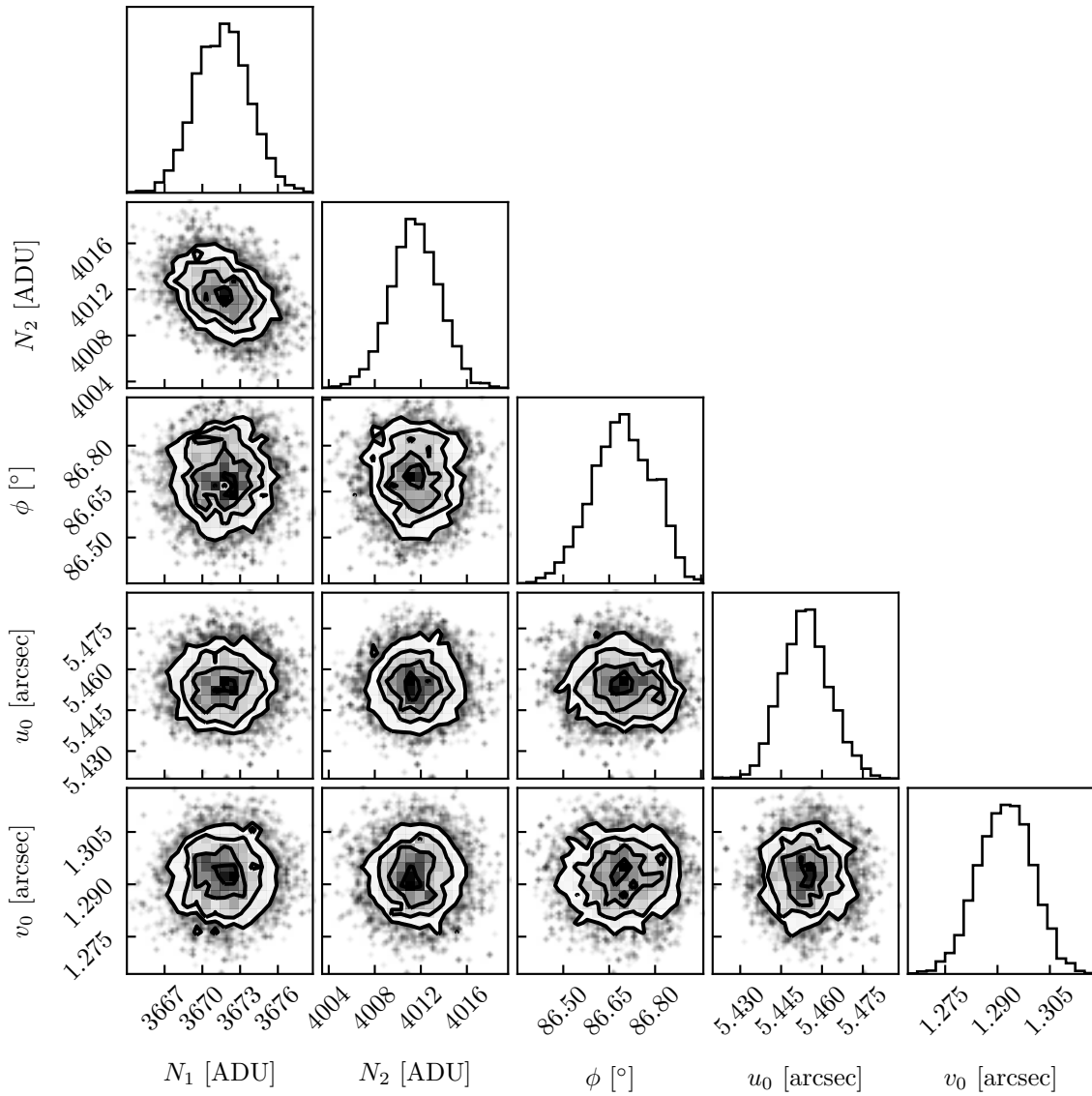
Figure 4.3: Posterior distributions and correlations of the fitting parameters for the interferometric image captured on Jupiter with baseline 8.0 mm. Sample size: 20000.
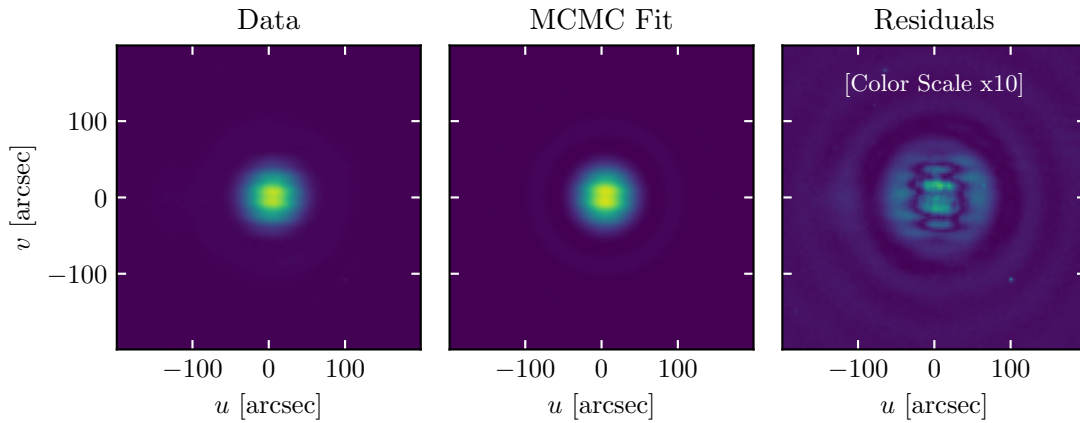

Figure 4.4: Example of data with MCMC-fitted model and residuals for the observation of Jupiter with baseline $B = 8.0$ mm.

B [mm]	N_1 [ADU]	N_2 [ADU]	ϕ [°]	u_0 [arcsec]	v_0 [arcsec]	Contrast
4.5	5276 ± 2	2468 ± 2	89.18 ± 0.02	1.16 ± 0.01	7.87 ± 0.01	0.3627 ± 0.0004
6.0	4386 ± 2	3581 ± 2	84.70 ± 0.06	0.55 ± 0.01	1.56 ± 0.01	0.1010 ± 0.0004
8.0	3672 ± 2	4012 ± 2	86.69 ± 0.10	5.45 ± 0.01	1.29 ± 0.01	-0.0442 ± 0.0005
10.5	3531 ± 2	3753 ± 2	87.44 ± 0.11	0.95 ± 0.01	-2.48 ± 0.01	-0.0305 ± 0.0005
13.5	3788 ± 2	3669 ± 2	84.88 ± 0.14	-1.41 ± 0.01	6.27 ± 0.01	0.0159 ± 0.0005
17.0	3672 ± 3	3678 ± 3	100 ± 40	-3.46 ± 0.01	2.09 ± 0.01	-0.0008 ± 0.0009
21.0	3808 ± 4	3808 ± 4	90 ± 50	-1.55 ± 0.01	3.63 ± 0.01	-0.0001 ± 0.0010

Table 4.1: Best fit parameters for Jupiter for each baseline as sampled by the MCMC algorithm.

B [mm]	N_1 [ADU]	N_2 [ADU]	ϕ [°]	u_0 [arcsec]	v_0 [arcsec]	Contrast
4.5	9638 ± 2	1533 ± 2	40.74 ± 0.01	8.44 ± 0.01	5.55 ± 0.01	0.7256 ± 0.0004
6.0	8442 ± 2	2815 ± 2	39.18 ± 0.02	0.41 ± 0.01	-1.16 ± 0.01	0.4998 ± 0.0004
8.0	6084 ± 3	4619 ± 2	48.51 ± 0.04	-9.14 ± 0.01	3.75 ± 0.01	0.1369 ± 0.0004
10.5	6233 ± 2	4501 ± 3	35.96 ± 0.05	5.61 ± 0.01	3.56 ± 0.01	0.1613 ± 0.0004
13.5	5287 ± 2	5604 ± 2	41.31 ± 0.06	-7.74 ± 0.01	-0.12 ± 0.01	-0.0290 ± 0.0004
17.0	5241 ± 3	5361 ± 2	43.52 ± 0.06	-5.84 ± 0.01	4.15 ± 0.01	-0.0113 ± 0.0004
21.0	5567 ± 3	5550 ± 2	43.30 ± 0.06	5.31 ± 0.01	5.32 ± 0.01	0.0015 ± 0.0004

Table 4.2: Best fit parameters for Mars for each baseline as sampled by the MCMC algorithm.

We can then transform each parameter vector in the sample to calculate the contrast according to Equation 2.13. This sample yields the mean and the statistical error for the contrast.

In summary, the parameters and their errors found by the MCMC sampler for each baseline on Jupiter and Mars are displayed in Table 4.1 and Table 4.2 along with the calculated contrasts.

4.3 Fitting the Visibility Function

The visibility $\mathcal{V}$ is the fringe contrast as a function of the mask baseline, shown in Figure 4.5. Using `samsam`, we can fit the theoretical model from Equation 2.15 to determine the angular diameter d of the planets. Additionally, we can anticipate some contrast loss introduced by the instrument and Earth's atmosphere, which we introduce by a global factor f, creating the following model function.

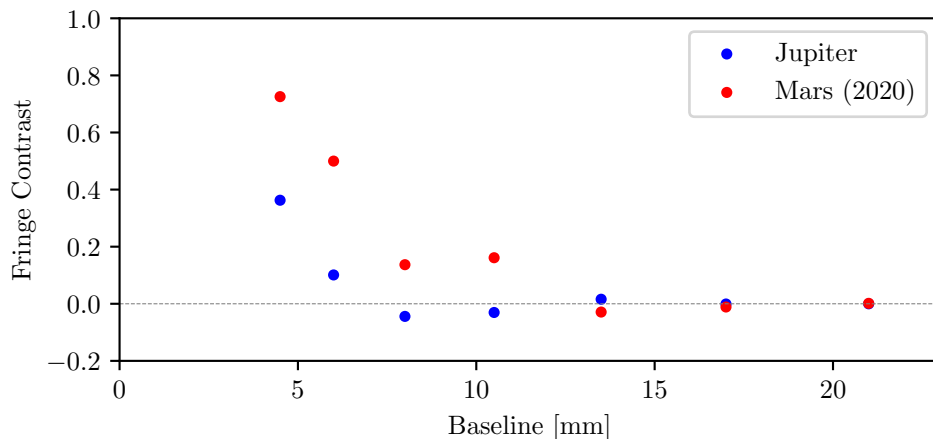$$\mathcal{V}_{d,f}(B) = f \times \frac{2J_1(\pi dB)}{\pi dB} \tag{4.5}$$

Figure 4.5: Sampled points of the visibility functions of the observed planets.

As before, we must define a loglikelihood function to feed the MCMC algorithm. We are again assuming Gaussian error distribution on the individual points, leading to the following loglikelihood.

$$\log L = -\frac{1}{2} \sum_i \log(2\pi\sigma_i^2) - \sum_i \frac{(\mathcal{V}_i - \mathcal{V}_{d,f}(B_i))^2}{2\sigma_i^2} \tag{4.6}$$

The standard deviation σ_i contains the statistical error on each contrast measurement determined by the fit on the images, which is displayed in Table 4.1 and Table 4.2 for Jupiter and Mars, respectively. In addition to this, the contrast is also subject to an external systematic uncertainty caused by the instrumentation and observing conditions, which we call σ_{ext}.

$$\sigma_i^2 = \sigma_{\text{stat},i}^2 + \sigma_{\text{ext}}^2 \tag{4.7}$$

However, since there is no way to quantify the complicated influence that the instrumentation error has on the contrast, we can estimate σ_{ext} as an additional parameter in the fit. Running the MCMC samples with 1 million samples produces the corner plot shown in Figure 4.6. We see that there are complicated correlation patterns present between the three parameters. Looking at the correlation between σ_{ext} and each of the other two parameters, we see that increasing σ_{ext} increases the spread of the sample in d or f. This is expected, since σ_{ext} describes the error bars on the data, whose size is correlated with the standard deviation of any physical parameters.
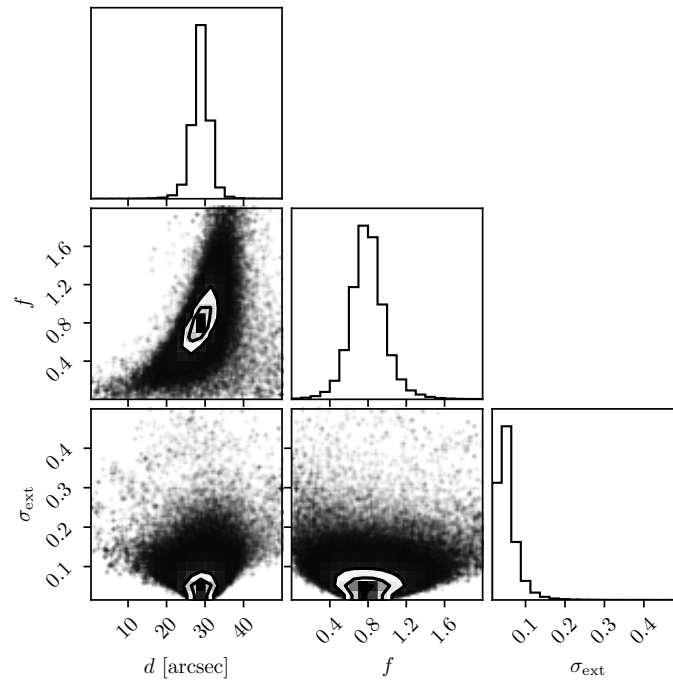
(a) Jupiter
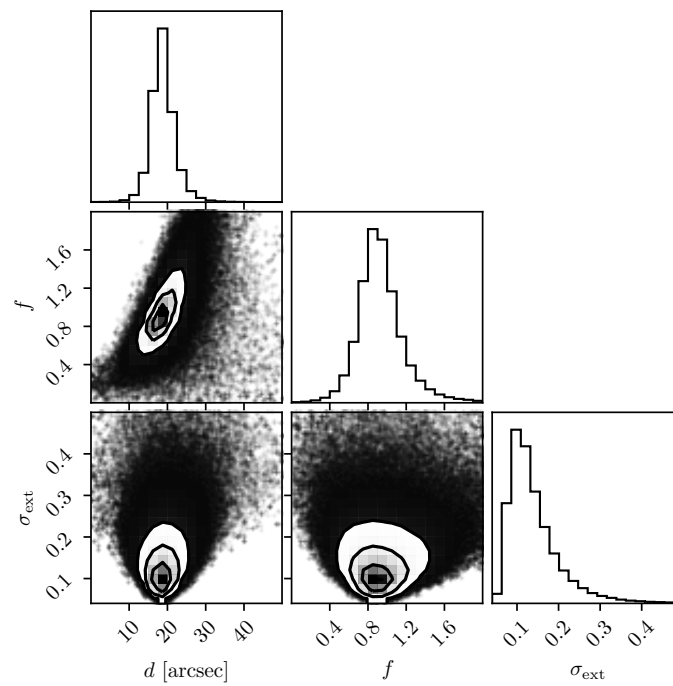
(b) Mars

Figure 4.6: Posteror distributions and correlations of the fitting parameters for the visibility function. Sample size: 1 000 000.

From this sampling we extract the best fit parameters shown in Table 4.3.

	Jupiter	Mars
d [arcsec]	28.8 ± 2.5	18.9 ± 3.4
f	0.80 ± 0.20	0.93 ± 0.24
σ_{ext}	0.05 ± 0.03	0.14 ± 0.06

Table 4.3: Best fit parameters for the visibility functions as sampled by the MCMC algorithm.
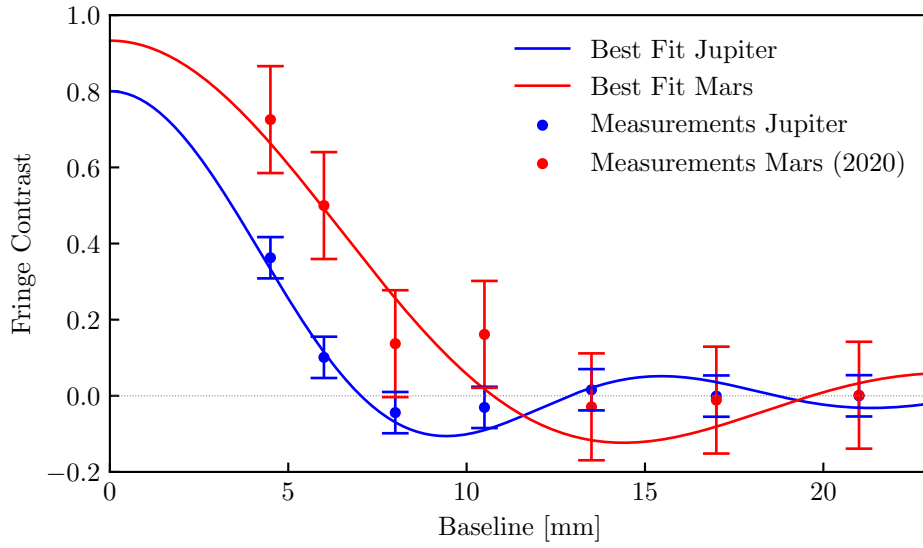
The best fit visibility curve is shown in Figure 4.7.

Figure 4.7: Sampled visibility functions with curve of best fit and σ_{ext} error bars.

Chapter 5

Results and Discussion

5.1 Summary of Results

The apparent angular diameters of Jupiter on the night of 12 December 2021 and Mars on the night of 18 November 2020 were determined to be

$$d_{\text{Jupiter}} = (28.8 \pm 2.5) \text{ arcsec}$$

$$d_{\text{Mars}} = (18.9 \pm 3.4) \text{ arcsec}$$

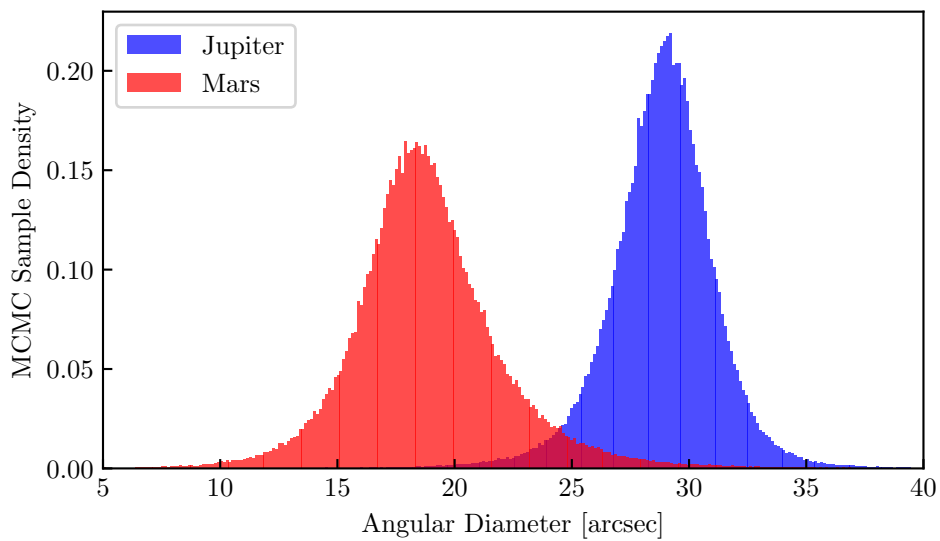Their distributions are shown in the histogram in Figure 5.1.

Figure 5.1: Sampled histogram of the angular diameter. Sample size: $1\,000\,000$.

At the time of observation, the true angular diameter of Jupiter viewed from Earth was 37.1 arcsec, the true angular diameter of Mars was 16.8 arcsec, as can be found online [6].

5.2 Discussion

What follows is a brief discussion of various aspects impacting the accuracy and precision of the results as well as an assessment of the validity of the interferometric method on TELESTO. We include some suggestions regarding possible points of improvement for future runs of this project.

Coherence Loss We have arbitrarily introduced the factor f to describe a global coherence loss caused by the instrumentation as well as atmospheric turbulence. Instead of fitting this as a global parameter on all baselines, we could measure it for each baseline at as the visibility at $Bd = 0$ by observing a point source such as a reference star. Then we could use these measurements to normalize the contrast on the planetary target. However, since moving the telescope possibly changes its effect on contrast reduction, this is likely not a viable method. Furthermore, this method would assume that coherence loss is linear, i.e. for constant instrumentational setup, the coherence loss is a fixed proportion of the contrast, an assumption which may not be valid.

Filter bandwidth During the entire project, we have modeled, simulated and analyzed the data assuming a monochromatic measurement with a wavelength λ. However, the observation was taken with a filter possessing a certain bandwidth of wavelengths, as stated in the technical details in Table 3.1. Accounting for this would necessitate integrating the involved models over the given wavelength range. Although this would complicate the math involved, it is in principle possible since the transmission spectra of astronomical filters are well defined [7].

Tracking error The inability of the telescope to track the position of a target over long exposure times is the main problem in this project. This effect also seems to be very unpredictable and is difficult to quantitatively propagate the induced error from the raw data through two MCMC fitting algorithms to analyze its effect on the planet diameter. It is even unknown whether the tracking issue affects the contrast measurement randomly or if there is some systematic component. Therefore, the estimated external error $\sigma_{\mathrm{ext}} = 0.05$ on the contrast likely does not account for the total instrumentational effect on the data.

Baseline Sample Ideally, we would require a larger set of baselines to accurately sample the visibility function. Especially the high-contrast domain at $B < 5\,\mathrm{mm}$ is lacking measurements. For apparently large objects such as Jupiter or Venus, it would be worth constructing masks with smaller baselines and smaller aperture diameters (e.g. $D = 2\,\mathrm{mm}$ and $B = 2.5\,\mathrm{mm}, 3.0\,\mathrm{mm}, 3.5\,\mathrm{mm}$). One could also use the rotation of the baselines to sample the visibility function in two dimensions, i.e. take multiple images with the same mask oriented at different angles.

Visibility Modeling The visibility function was modeled on the assumption that the planets appear as perfect homogeneous circles. This is a gross simplification that may have impacted the

accuracy of the result. For example, Jupiter possesses cloud patterns whose reflection coefficient is highly inhomogeneously distributed latitudinally. The planets may not necessarily be visible in full phase at any one time and are affected by limb darkening (especially Jupiter). One could extend the model of the planets by introducing additional parameters describing the spatial brightness distribution. Building on the previous point, this would then involve sampling the visibility at many more baselines at different angles in order to obtain an accurate result. While this is feasible in theory, it would require much more computation time, given that it takes a standard PC around the order of 20 minutes to obtain a single reliable contrast measurement from an image.

Result discrepancy   The measurement for Mars is 13% larger than its true diameter, which is within the 1σ interval. We obtain a result for Jupiter that is 22% smaller than the true size of Jupiter. This corresponds to a much worse discrepancy of around 3.3σ. This points to some fault in the instrumentation or model that is unaccounted for in the external error. Most likely, it can be attributed to the fact that Jupiter is brighter in the center than around the edges, and the tracking issue which would blur the edges, making the effective radius within which Jupiter is at maximum intensity even smaller.

Precision   The diameter was obtained with a precision of a few arcseconds. At a pixel size of 0.8, arcsec, this roughly corresponds to the same precision achievable by direct imaging on TELESTO. However, it must be stated that without the dominating external instrumentational error, the contrast was measured precisely to the order of $\pm\,0.05\%$ (Table 4.1/Table 4.2), which underlines the extreme precision achievable by interferometry on professional instrumentation.

Bibliography

[1] J. -M. Mariotti. "Introduction to Fourier Optics and Coherence." In: *Diffraction-Limited Imaging with Very Large Telescopes*. Ed. by D. M. Alloin and J. -M. Mariotti. Vol. 274. NATO Advanced Study Institute (ASI) Series C. Jan. 1989, p. 3.

[2] Don Cross. *Solar System Calculator*. URL: http://cosinekitty.com/solar_system.html (visited on 01/13/2022).

[3] *Astronomy Seeing Versoix*. Meteoblue. URL: https://www.meteoblue.com/en/weather/outdoorsports/seeing/versoix_switzerland_2658151.

[4] Jean-Baptiste Delisle. *samsam: Scaled Adaptive Metropolis SAMpler*. Université de Genève. URL: https://gitlab.unige.ch/Jean-Baptiste.Delisle/samsam.

[5] Daniel Foreman-Mackey. "corner.py: Scatterplot matrices in Python." In: *The Journal of Open Source Software* 1.2 (June 2016), p. 24. DOI: 10.21105/joss.00024. URL: https://doi.org/10.21105/joss.00024.

[6] *Distance, Brightness, and Size of Planets*. Time and Date. URL: https://www.timeanddate.com/astronomy/planets/distance.

[7] Wikipedia. *Photometric system*. 2021. URL: https://en.wikipedia.org/wiki/Photometric_system.